Wavelength dependence of photoelectron momentum distributions in a spatially inhomogeneous field

Yue Sun, Zhuo Wang, Xiao-Xin Huo, and Xue-Shen Liu*
Institute of Atomic and Molecular Physics, Jilin University, Changchun 130012, People's Republic of China

(Received 10 January 2022; revised 16 March 2022; accepted 14 April 2022; published 25 April 2022)

The effect of the spatial inhomogeneity on the photoelectron momentum distributions (PMDs) is recently identified [Chen *et al.*, Phys. Rev. A **104**, 043107 (2021)]. As an important parameter of the laser field, the wavelength cannot be ignored. We theoretically investigate the wavelength dependence of the PMDs in a spatially inhomogeneous field. The results show that the PMDs gradually move to the negative direction with the increase of the laser wavelength compared with the case of the spatially homogeneous field. However, a critical value of the wavelength appears, where the PMDs are just separated. Then, the PMDs can be clearly separated into two regions and the rescattering energy of the electron is tremendously enhanced. We illustrate that the holographic interference structure can be isolated in the relative high-energy region and the holographic interference structure for the shorter wavelength is more obvious. A prominent high-energy peak appears in the critical wavelength and the high-energy peak is sensitive to the initial transverse momentum of the rescattering electrons after tunneling. Moreover, we also demonstrate that the critical wavelength will change with the inhomogeneity parameters.

DOI: 10.1103/PhysRevA.105.043115

I. INTRODUCTION

Strong-field atomic ionization is one of the most important processes in ultrafast physics, which triggers many interesting nonlinear phenomena, such as above-threshold ionization (ATI) [1–5], high-order harmonic generation (HHG) [6–9], and nonsequential double ionization [10–13]. These processes can be interpreted by the three-step model [14], i.e., ionization, acceleration in the strong laser field, and return to the parent nucleus. According to the quantum orbit theory [15], the ionized electron wave packets (EWPs) have many different propagation paths. They can directly reach the detector (known as direct electron) or return to the parent ion for rescattering (known as rescattering electron) depending on the tunneling ionization time.

The EWPs ionized from different ionization time with the same final momentum will interfere with each other. There are various interesting interference structures in the photoelectron momentum distributions (PMDs) [16]. The ATI rings [17], the temporal double-slit interference [18], and the photoelectron holography [19] have been theoretically and experimentally demonstrated. The photoelectron holography is considered an ideal method to probe ultrafast atomic and molecular dynamics in a strong laser field due to recording time-resolved information about both the electron and the ion. Thus, the separation of photoelectron holography from other interference structures has become a hot topic in recent years [20,21].

The field enhancement in the vicinity of metallic nanostructures has attracted much attention both experimentally [22] and theoretically [23]. The enhanced field is not spatially homogeneous, and is called the spatially inhomogeneous field. Compared with the spatially homogeneous field, the spatially inhomogeneous field shows a strong spatial gradient, thus the ionized electrons can obtain higher energy [24], the cutoff of the HHG can be extended [23,25,26], and the ultrashort isolated attosecond pulse can be generated [27,28]. In addition, the spatially inhomogeneous field also plays an important role in the ATI process. The trajectory of the electron and the energy spectra can be precisely modulated [29,30].

In the past few decades, the HHG and ATI in the inhomogeneous field are investigated. However, there are few investigations on the PMDs [31]. Recently, the PMDs for a hydrogen atom ionized in the inhomogeneous field was demonstrated using the time-dependent Schrödinger equation (TDSE) and the classical trajectory model. It is found that the rescattering energy of the electron is greatly enhanced and the electronic wave packet is separated in momentum space [32]. As an important parameter, the laser wavelength has been widely studied in the homogeneous field and in the inhomogeneous field [33–37]. The distinctive wavelength-dependent features of the PMDs may provide a way to design high-energy nanometer-sized ultrafast electron sources. Thus, it is necessary to explore the wavelength dependence of the PMDs in the inhomogeneous field.

In this paper, we theoretically investigate the wavelength dependence of the photoelectron momentum distribution of hydrogen atoms in a few-cycle inhomogeneous field. Based on the improved semiclassical two-step (ISCTS) model, we find that the PMDs can be separated into two regions when the wavelength reaches a certain value in the inhomogeneous field, which is called the critical wavelength. We can observe that the rescattering energy of the electron is much higher in the spatially inhomogeneous field than that in the spatially homogeneous field. When the wavelength is longer than the critical wavelength, the increase of the rescattering

*liuxs@jlu.edu.cn

energy is significant. Based on the electron orbits analysis, we demonstrate that the high-energy region mainly originates from the short orbit of the rescattering electrons. We also demonstrate that the holographic interference structure can be isolated in the inhomogeneous field. And the holographic interference structure of the shorter wavelength is more obvious than that of the longer wavelength. Our results may provide a reference for further analytical research of the holographic interference in a few-cycle inhomogeneous field. In addition, a prominent high-energy peak appears in the critical wavelength and the high-energy peak is sensitive to the initial transverse momentum of the rescattering electrons after tunneling. Moreover, we demonstrate that the critical wavelength is gradually decreased as the inhomogeneity parameter increases. Throughout the paper, we demonstrate that not only the intensity of the inhomogeneous field will affect the PMDs, but also the effect of wavelength cannot be ignored.

II. THEORETICAL MODEL AND COMPUTATIONAL METHODS

In this section, we briefly introduce the quantum trajectory Monte Carlo (QTMC) method [38] and the semiclassical two-step (SCTS) model [39], which are the semiclassical methods. For the spatial inhomogeneity field, the nondipole effect should be considered [40]. In this paper, the spatial gradient of the spatially inhomogeneous field we used is small and the photon energy $E \ll 1$ keV. Thus the dipole approximation can still be justified [40]. The free electron will be affected by the electric field and magnetic field [41]. The equation of motion for the free electron is $\vec{F} = q\vec{E} + q\vec{v} \times \vec{B}$, where $q\vec{E}$ is the electric field force and $q\vec{v} \times \vec{B}$ is the magnetic field force (i.e., Lorentz force). Because the intensity of the magnetic field is many orders of magnitude lower than that of the electric field, we also neglect the magnetic field of the laser field. Thus we ignore the nondipole effect and the magnetic field of the laser field.

The first step of the QTMC is the tunneling ionization in a quasistatic laser field. After tunneling, the electron motion in the Coulomb and laser fields is described by the Newton equation

$$\ddot{\vec{r}}(t) = \frac{-\vec{r}(t)}{r^3(t)} - \vec{E}(\vec{r}, t), \tag{1}$$

where r is the distance between the ionized electron and the nucleus and $\vec{E}(\vec{r}, t)$ is the external spatially inhomogeneous field. It is worth noting that there are different forms of the inhomogeneous field [25,27,32] due to the different shapes of the metallic nanostructures. In this paper, we select a widely used laser field that decays exponentially in the vicinity of a nanotip. It is approximated as linearly decreasing,

$$\begin{aligned}\vec{E}(\vec{r}, t) &= (1 + 2\varepsilon x)E_0 f(t)\sin(\omega t)\hat{x} \\ &= (1 + 2\varepsilon x)E(t)\hat{x},\end{aligned} \tag{2}$$

where $\hat{x}$ is the direction of laser polarization, E_0 denotes the field amplitude, $f(t) = \sin^2(\frac{\pi t}{nT})$ is the envelope pulse with the parameter $n = 4$, $T = \frac{2\pi}{\omega}$ is the optical cycle, and ω is the laser frequency. Compared with the homogeneous field, ε is a unique parameter of the inhomogeneous field. It represents the degree of the spatial inhomogeneity and $2\varepsilon = 1/l_F$, where l_F is the decay length. Here the inhomogeneity parameter ε is chosen to be 0.003.

In a two-dimensional $P_x \times P_y$ plane, we put the electrons into a bin if their asymptotic momenta are very close. The probability of each bin can be expressed as

$$|A|^2_{\text{bin}} = \left| \sum_j \sqrt{W(t_0, v_{0,\perp})}\exp(-i\Phi) \right|^2, \tag{3}$$

where j denotes the jth ionized electron trajectory and $W(t_0, v_{0,\perp})$ denotes the Ammosov-Delone-Krainov rate [42,43],

$$W(t_0, v_{0,\perp}) \sim \exp\left[-\frac{2k^3}{3E(t_0)}\right]\exp\left[-\frac{kv^2_{0,\perp}}{E(t_0)}\right], \tag{4}$$

where t_0 denotes the ionization time, $v_{0,\perp}$ denotes initial transverse velocity, and $k = \sqrt{2I_p}$.

In the QTMC model, the trajectory phase in the homogeneous field for each electron is

$$\Phi = \int_{t_0}^{\infty}\left[\frac{v(t)^2}{2} - \frac{Z}{r(t)} + I_p\right]dt, \tag{5}$$

where $v(t)$ is the ionized electron velocity, Z is the ion charge, and I_p is the ionization potential.

For the trajectory phase for each electron, Shvetsov-Shilovski *et al.* came up with a SCTS model. We can find the specific description of the SCTS model in Ref. [39]; the phase in the homogeneous field can be modified as

$$\begin{aligned}\Phi &= -\vec{v}_0 \cdot \vec{r}_0(t_0) + I_p t_0 \\ &\quad - \int_{t_0}^{\infty}\{\dot{\vec{p}}(t) \cdot \vec{r}(t) + H[\vec{r}(t), \vec{p}(t)]\}dt \\ &= -\vec{v}_0 \cdot \vec{r}_0(t_0) + I_p t_0 - \int_{t_0}^{\infty}\left[\frac{v(t)^2}{2} - \frac{2Z}{r(t)}\right]dt,\end{aligned} \tag{6}$$

where $\dot{p}(t)$ is expressed in terms of the negative gradient of the total potential containing the electric field and the Coulomb potential, $H[\vec{r}(t), \vec{p}(t)]$ is the Hamiltonian function,

$$H[\vec{r}(t), \vec{p}(t)] = \frac{p^2(t)}{2} + V_{\text{laser}}(\vec{r}, t) + V(\vec{r}), \tag{7}$$

where $V(\vec{r})$ is the atomic potential, and $V_{\text{laser}}(\vec{r}, t) = \vec{E}(t) \cdot \vec{r}(t)$ represents the potential of the laser-atom interaction in the homogeneous field. It is worth noting that $\dot{p}(t)$ and the potential of the laser-atom interaction will change in the inhomogeneous field of linear approximation [32]

$$\begin{aligned}V_{\text{laser}}(\vec{r}, t) &= \int_0^{\vec{r}} d\vec{r} \cdot \vec{E}(\vec{r}, t) \\ &= E(t)x(1 + \varepsilon x).\end{aligned} \tag{8}$$

The Hamiltonian function can be improved as

$$H[\vec{r}(t), \vec{p}(t)] = \frac{p^2(t)}{2} + E(t)x(1 + \varepsilon x) + V(\vec{r}). \tag{9}$$

To avoid the unphysical effect, we take the same approximation as in Ref. [32], so that the laser field is zero in the region

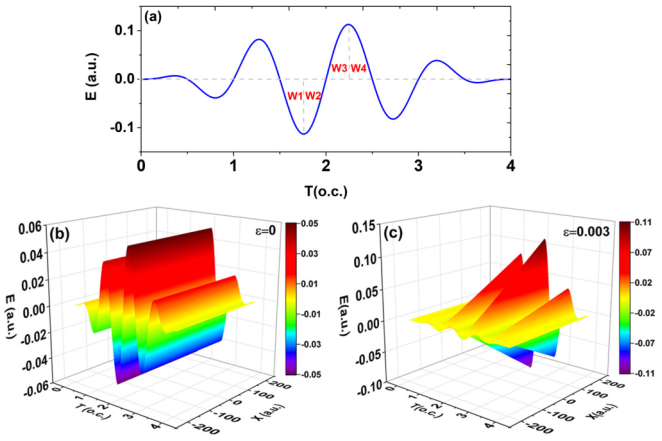

FIG. 1. (a) Temporal shape of the laser field. (b) Three-dimensional coupling field of the homogeneous laser field ($\varepsilon = 0$) in time and space. (c) Three-dimensional coupling field of the inhomogeneous laser field ($\varepsilon = 0.003$) in time and space.

of $x < -1/2\varepsilon$. Finally, the phase in the inhomogeneous field can be improved as

$$\Phi = -\vec{v}_0 \cdot \vec{r}_0(t_0) + I_p t_0 - \int_{t_0}^{\infty} \left[\frac{p(t)^2}{2} - \frac{2Z}{r(t)} - \varepsilon x^2 E(t) \right] dt, \tag{10}$$

where $r = \sqrt{x^2 + y^2}$. We call it ISCTS. We use the phase of Eq. (10) to investigate the ionization progress in the inhomogeneous field and we use atomic units throughout this paper.

III. RESULTS AND DISCUSSIONS

Figure 1(a) shows the temporal shape of the laser field. For a few-cycle laser pulse, there is an optical period that plays a significant role in the PMDs, which is indicated as the different ionized time windows W1–W4. We define windows W1+W2 as the first half cycle and the windows W3+W4 as the second half cycle. Figures 1(b) and 1(c) show the three-dimensional coupling field of the homogeneous laser field ($\varepsilon = 0$) and the inhomogeneous laser field ($\varepsilon = 0.003$) in time and space, respectively. We can see that the field strength is a constant in space in the homogeneous laser field ($\varepsilon = 0$) as shown in Fig. 1(b). However, the field strength is amplified from the beginning to the end of the simulation box in the inhomogeneous laser field ($\varepsilon = 0.003$) as shown in Fig. 1(c). Due to the enhanced field, the PMDs will be modulated. Next, we will illustrate the wavelength dependence of the PMDs in this enhanced field.

Figure 2 shows the PMDs of the H atom for different laser wavelengths in the spatially homogeneous field ($\varepsilon = 0$) and the spatially inhomogeneous field ($\varepsilon = 0.003$). The peak intensity of the laser pulse is $I_0 = 1\times10^{14}$ W/cm^2. Figures 2(a1)–2(a6) show that the PMDs have little changes

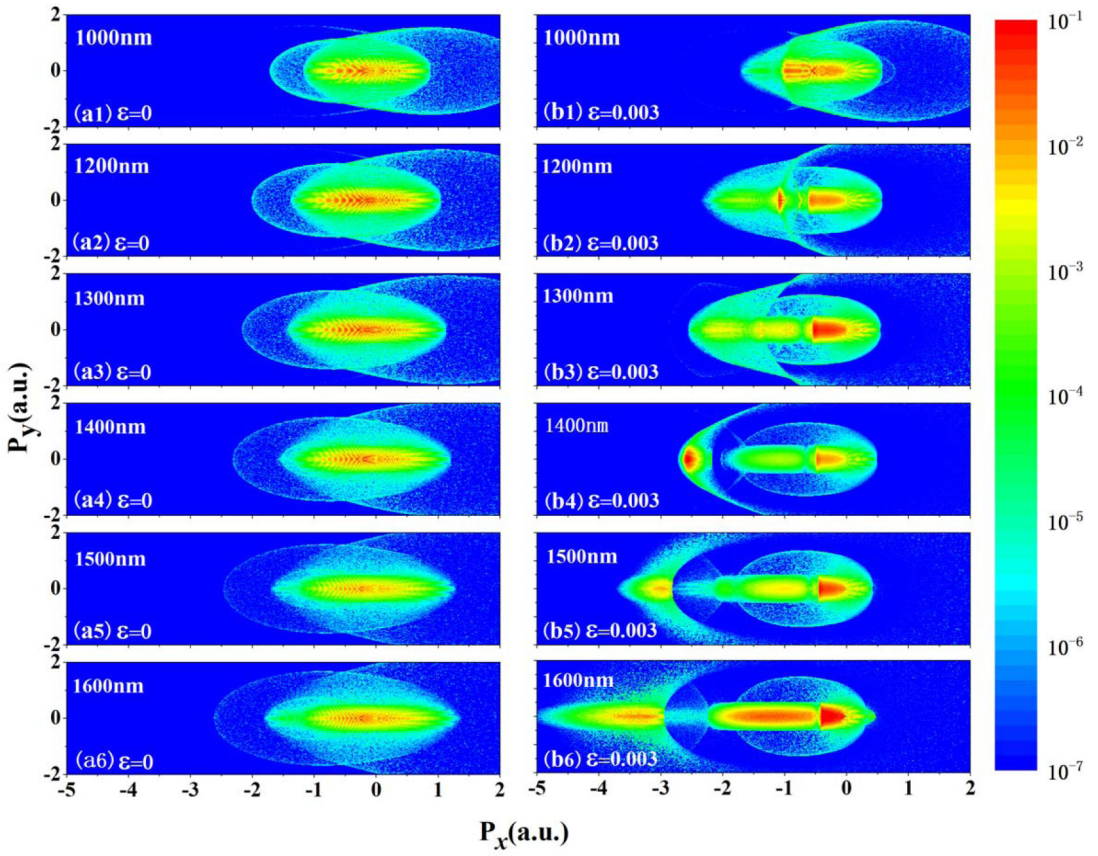

FIG. 2. Two-dimensional photoelectron momentum distributions for different laser wavelengths (from $\lambda = 1000$ nm to $\lambda = 1600$ nm) (a1)–(a6) in the spatially homogeneous field ($\varepsilon = 0$) and (b1)–(b6) in the spatially inhomogeneous field ($\varepsilon = 0.003$).

with the increase of the wavelength in the spatially homogeneous field ($\varepsilon = 0$). However, Figs. 2(b1)–2(b6) show that the PMDs have obvious changes with the increase of the wavelength in the spatially inhomogeneous field ($\varepsilon = 0.003$).

Figure 2(b1) indicates that the PMDs are distributed in the region of $p_x \in [-1.6$ a.u, 0.6 a.u.] for the wavelength $\lambda = 1000$ nm. It can be seen that the PMDs gradually move to the negative direction and separate into two regions as the wavelength increases from $\lambda = 1000$ nm to $\lambda = 1600$ nm in the spatially inhomogeneous field. Figure 2(b6) indicates that the PMDs can reach $p_x = -5$ a.u. for the wavelength $\lambda = 1600$ nm in the spatially inhomogeneous field, which is in good agreement with the TDSE result [Fig. 1(c)] and the classical model result [Fig. 1(e)] of Ref. [32]. It indicates that the electronic wave packet can obtain high energy in the spatially inhomogeneous field, and the longer the wavelength is, the more energy the electronic wave packet could obtain.

Figure 2(b4) shows that the PMDs can be separated into two regions for the wavelength $\lambda = 1400$ nm in the spatially inhomogeneous field. The critical wavelength appears. When the wavelength is shorter than this critical wavelength, the PMDs are distributed in the continuous region as shown in Figs. 2(b1)–2(b3). However, when the wavelength is longer than this critical wavelength, the PMDs are separated into two parts as shown in Figs. 2(b5) and 2(b6), i.e., the relative high-energy region and the relative low-energy region can be well separated in the longer wavelength. And these two regions represent the electronic wave packet ionized in different half cycles [32].

By comparing the PMDs in the spatially homogeneous field and the spatially inhomogeneous field, we can find that the holographic interference structure can be isolated from various interference structures in the spatially inhomogeneous field. The holographic structure will not be obvious at the longer wavelength. This is because the number of direct electrons increases and the number of the rescattered electrons decreases with the increase of the wavelength, which is in good agreement with that demonstrated in Ref. [37]. In addition, the holographic structure is mainly concentrated in the left part (relative high-energy region) of the PMDs as shown in Fig. 2(b1).

Figure 2(b1) shows that the PMD is uniform for the wavelength $\lambda = 1000$ nm. With increasing the laser wavelength, the PMDs distributed in the right part (relative low-energy region) are stronger than that in the left part (relative high-energy region) as shown in Figs. 2(b2) and 2(b3) and Figs. 2(b5) and 2(b6) for the wavelengths $\lambda = 1200$ nm, $\lambda = 1300$ nm, $\lambda = 1500$ nm, and $\lambda = 1600$ nm. [We ignore the small differences in Fig. 2(b2).] However, for the critical wavelength $\lambda = 1400$ nm, the PMDs have the stronger distribution in the relative high-energy region as shown in Fig. 2(b4). In summary, these phenomena indicate that the PMDs are very sensitive to the wavelength in the inhomogeneous field.

We know that the momentum and energy of the electrons are dependent on the initial ionization time of the electrons [32,44]. To clarify the physical mechanism of the wavelength dependence of the PMDs in the spatially inhomogeneous field, we investigate the energy distribution of photoelectrons with respect to the ionization time for different wavelengths as shown in Fig. 3. We focus on two yellow dotted line regions as indicated in Fig. 3, which correspond to the first half cycle (1.5–2.0 T, windows W1+W2) and the second half cycle (2.0–2.5 T, windows W3+W4) of the electric field as shown in Fig. 1(a). When the wavelength is shorter than the critical wavelength, Figs. 3(a)–3(c) show that there is a positive slope in the first half cycle and a negative slope in the second half cycle for the energy distribution of photoelectrons, and the electronic wave packets are mainly released from the time windows W2 and W3. We can clearly observe that the energy gradually increases in the first half cycle, i.e., the electronic wave packet ionized at the later time can obtain more energy in the first half cycle. Similarly, the electronic wave packet ionized at the earlier time can obtain more energy in the second half cycle.

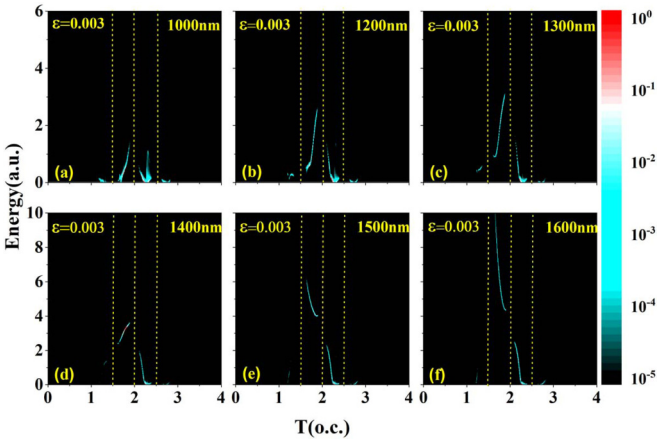

FIG. 3. Energy distribution of photoelectrons with respect to the ionization time for different wavelengths in the spatially inhomogeneous field ($\varepsilon = 0.003$). (a) $\lambda = 1000$ nm, (b) $\lambda = 1200$ nm, (c) $\lambda = 1300$ nm, (d) $\lambda = 1400$ nm, (e) $\lambda = 1500$ nm, and (f) $\lambda = 1600$ nm.

Figures 3(a)–3(c) also show that the slopes and the final energy of the electrons from the first half cycle and the second half cycle increase with the increase of the wavelength. However, when the wavelength is increased to the critical wavelength ($\lambda = 1400$ nm), the slope decreases as shown in Fig. 3(d). It is worth noting that the final energy of the electrons still increases, the maximum energy can reach to Energy ≈ 4.0 a.u., and the lowest energy in the first half cycle is higher than the highest energy in the second half cycle. As a result, the high-energy region and the low-energy region can be well separated in this critical wavelength, which is in agreement with that shown in Fig. 2(b4). The electronic wave packets ionized within the first half cycle are concentrated in the relative high-energy region and the electronic wave packets ionized within the second half cycle are concentrated in the relative low-energy region, which is in agreement with that demonstrated in Ref. [32].

When the wavelength is longer than this critical wavelength, Figs. 3(e) and 3(f) show that the final energy of the electrons has vastly improved. Figure 3(f) shows that the maximum energy can reach to Energy ≈ 10 a.u. for the wavelength $\lambda = 1600$ nm, which is much higher than that shown in Figs. 3(d) and 3(e) for the wavelengths $\lambda = 1400$nm and $\lambda = 1500$ nm. Most important of all, the slope of the energy

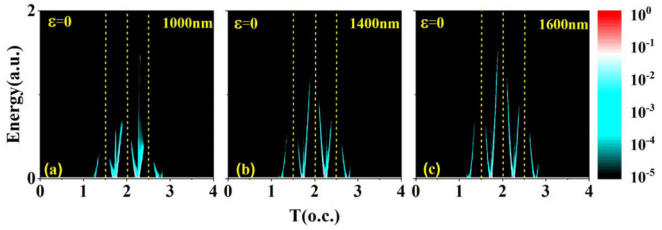

FIG. 4. Energy distribution of photoelectrons with respect to the ionization time for different wavelengths in the spatially homogeneous field ($\varepsilon = 0$). (a) $\lambda = 1000$ nm, (b) $\lambda = 1400$ nm, and (c) $\lambda = 1600$ nm.

distribution of photoelectrons reverses, i.e., the slope of the energy distribution of photoelectrons in the first half cycle is negative as shown in Figs. 3(e) and 3(f). However, the slope of the energy distribution of photoelectrons in the second half cycle remains unchanged. This indicates that the dynamics of the electrons are very sensitive to the wavelength in the first half cycle and the electronic wave packet ionized at an earlier time can obtain more energy in the first half cycle. In addition, the time windows of ionized electronic wave packets are extended from W2 to W1+W2 in the first half cycle, which is in agreement with that demonstrated in Ref. [32].

In order to better understand the reason for the slope transition, we also investigate the energy distribution of photoelectrons with respect to the ionization time for three special wavelengths, which are the critical wavelength ($\lambda = 1400$ nm), shorter than the critical wavelength ($\lambda = 1000$ nm), and longer than the critical wavelength ($\lambda = 1600$ nm) in the homogeneous field ($\varepsilon = 0$) as shown in Fig. 4.

In Fig. 4(a), we show the energy distribution of photoelectrons for the laser wavelength $\lambda = 1000$ nm in the spatially homogeneous field ($\varepsilon = 0$). There are positive slopes before the laser peaks and negative slopes after the laser peaks for the first half cycle and the second half cycle, which is similar to the result of Fig. 2(c) in Ref. [44]. In the spatially homogeneous field, the direct electrons released from the rising edge of the laser field and the rescattering electrons released from the falling edge of the laser field. In the combined Coulomb and laser field, the energy of the direct electrons gradually decreases and the energy of the rescattering electrons gradually increases. Therefore, there is a change of the positive and the negative slopes in each half cycle.

In Figs. 4(b) and 4(c), we show the energy distribution of photoelectrons in the spatially homogeneous field ($\varepsilon = 0$) for the laser wavelengths $\lambda = 1400$ nm and $\lambda = 1600$ nm, respectively. We can clearly observe that the general structure has not changed; only slight differences exist for the maximum energy. We can see that the maximum energy is from Energy ≈ 0.6 a.u. as shown in Fig. 4(a) to Energy ≈ 1.5 a.u. as shown in Fig. 4(c).

Compared with the case of the spatially homogeneous field, it implies that the dynamics of the electronic wave packets are more sensitive to the wavelength in the spatially inhomogeneous field than to that in the spatially homogeneous field. The longer the wavelength, the more energy the electronic wave packet could obtain in the spatially inhomogeneous field. In the inhomogeneous field, there is a spatial adiabaticity parameter [36] $\delta = l_F/l_q$, where l_F is the decay length and $l_q = eE/m\omega^2$ is the quiver amplitude. According to this parameter, a longer wavelength means that the electronic wave packet feels a stronger field amplitude of the spatially inhomogeneous field. Thus, for the longer wavelength, the electronic wave packet can obtain higher energy [37].

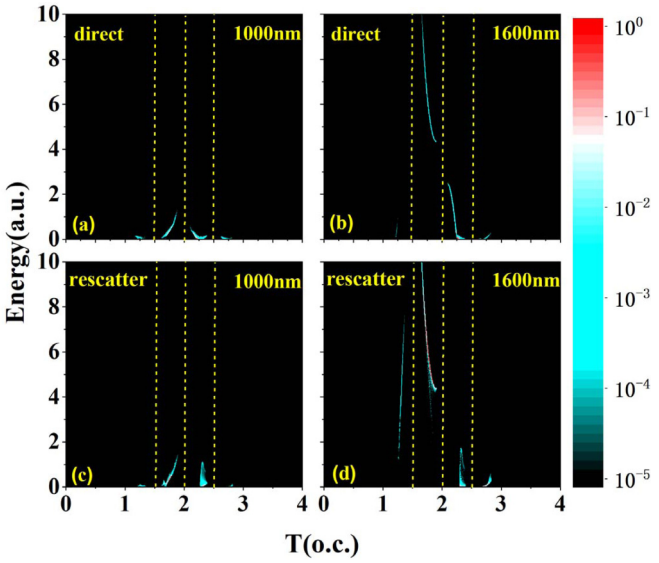

FIG. 5. Energy distribution of the direct electrons and the rescattering electrons with respect to the ionization time when the laser wavelength is shorter and longer than the critical wavelength in the spatially inhomogeneous field ($\varepsilon = 0.003$). (a) and (c) The laser wavelength ($\lambda = 1000$ nm) is shorter than the critical wavelength; (b) and (d) the laser wavelength ($\lambda = 1600$ nm) is longer than the critical wavelength. Upper panel: energy distributions of the direct electrons; lower panel: energy distributions of the rescattering electrons.

To obtain the dynamics of different kinds of electrons in the inhomogeneous field ($\varepsilon = 0.003$), we show the energy distribution of the direct electrons and the rescattering electrons with respect to the ionization time when the laser wavelength is shorter and longer than the critical wavelength in Fig. 5. The electron orbits can be classified as the direct orbit and the rescattering orbit according to the effect of the Coulomb potential on them [21,33,45]. If $p_\perp v_{\perp 0} > 0$ (where $p_\perp$ is the final perpendicular momentum and $v_{\perp 0}$ is the initial velocity), we believe that the Coulomb potential is weak, where the Coulomb potential is not strong enough to change the perpendicular direction of the electron orbit, and this type of ionized orbit is called the direct orbit. Similarly, if $p_\perp v_{\perp 0} < 0$, we believe that the Coulomb potential is strong, and this type of ionized orbit is called the rescattering orbit.

From Fig. 5, we can clearly observe that the direct electrons and the rescattering electrons have the same ionization time and the same energy growth trend when the laser wavelength is shorter than the critical wavelength ($\lambda = 1000$ nm) and longer than the critical wavelength ($\lambda = 1600$ nm) in the first half cycle. However, only direct electrons can be found in the

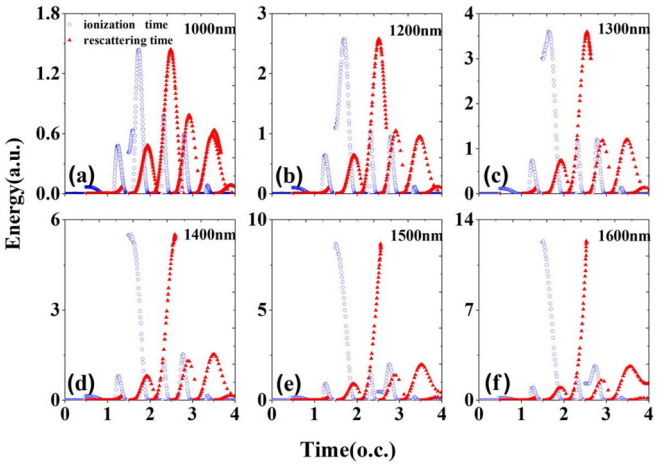

FIG. 6. Rescattering energies of electrons as a function of the ionization time (blue hollow circle) and rescatteing time (red solid triangle) for different laser wavelengths in the spatially inhomogeneous field ($\varepsilon = 0.003$).

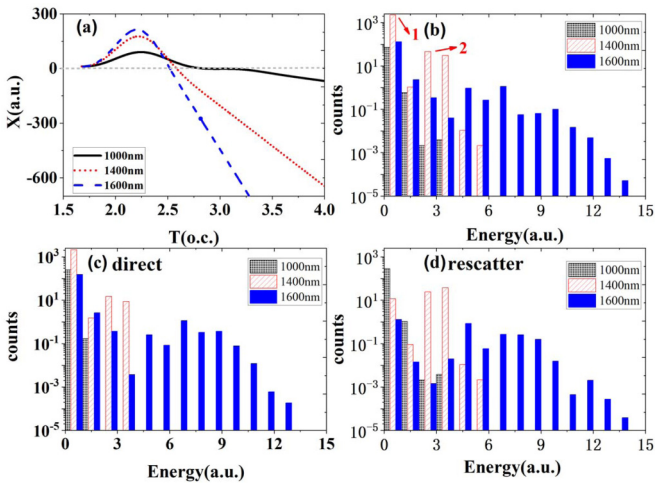

FIG. 7. (a) The evolution of the classical trajectories for different wavelengths in the spatially inhomogeneous field ($\varepsilon = 0.003$). (b)–(d) Histogram of the counts of the photoelectron as a function of the final energy in the spatially inhomogeneous field ($\varepsilon = 0.003$) for three different wavelengths $\lambda = 1000$ nm, $\lambda = 1400$ nm, and $\lambda = 1600$ nm, respectively. (b) All electrons, (c) the direct electrons, and (d) the rescattering electrons.

second half cycle. We ignore the influence of the electrons ionized during the window W4 due to the lower final energy.

We know that the holographic structure stems from the rescattering and the direct electron wave packet ionized at the same quarter of the laser field. Therefore, this phenomenon strongly proves that the holographic structure is mainly concentrated in the relative high-energy region as shown in Figs. 2(b1)–2(b6).

To clarify the physical mechanism of the wavelength dependence of electrons in the inhomogeneous field, we trace the orbits of the rescattering electrons based on the three-step model [14]. Figure 6 shows the rescattering energies of the electrons as a function of the ionization time (blue hollow circle) and the rescattering time (red solid triangle) for different laser wavelengths in the spatially inhomogeneous field ($\varepsilon = 0.003$). When the laser wavelength is shorter than the critical wavelength $\lambda = 1400$ nm, Figs. 6(a)–6(c) show that the long orbit and the short orbit contribute to the rescattering energies. The electrons ionized during the first half cycle can obtain the high rescattering energies and the rescattering energies will increase with the increase of the wavelength. We also observe that the contribution of the long orbit will wear off with the increase of wavelength.

Figure 6(d) shows that the main electron orbits that contribute to the rescattering energies are short orbits for the critical wavelength $\lambda = 1400$ nm. Subsequently, due to the electron wave packet diffusion effect [46], Figs. 6(e) and 6(f) show that there are only short orbits; the long orbits have disappeared. For these short orbits, we can observe that the electrons ionized at the earlier time and recombined at the later time can obtain more energy in the inhomogeneous field, which is in good agreement with the results of Figs. 3(e) and 3(f).

In order to better illustrate that the electron can obtain the high energy in the first half cycle and the dramatic change of the energy distribution in Fig. 5, we trace the classical trajectories of the electron for different wavelengths $\lambda = 1000$ nm (black solid line), $\lambda = 1400$ nm (red dotted line), and $\lambda = 1600$ nm (blue dashed line) as shown in Fig. 7(a). We can observe that the electrons ionized during 1.5–2.0 T (i.e., the first half cycle) all move into the positive semiaxis of the x axis, and with the increase of wavelength, the distance of electron movement on the positive semiaxis of the x axis increases. For the linear approximation of the spatial inhomogeneous field, the field strength gradually increases on the positive semiaxis of the x axis as shown in Fig. 1(c). The electron is subjected to a stronger electric field if the distance of the electron moves farther away [32]. This proves why the electron can obtain the higher energy for the longer wavelength in the first half cycle. When the lowest energy in the first half cycle is higher than the highest energy in the second half cycle, the critical wavelength appears.

In order to understand the physical origin of the stronger distribution in the relative high-energy region shown in Fig. 2(b4), we investigate the photoelectron energy spectrum, which is the universal method in strong-field ionization [30,37,47]. We present the histogram of the counts of the photoelectron as a function of the final energy for all electrons [Fig. 7(b)], the direct electrons [Fig. 7(c)], and the rescattering electrons [Fig. 7(d)] for three different wavelengths. In Fig. 7(b), we can find two anomalous high-energy peaks as indicated by the arrows 1 and 2 for the critical wavelength $\lambda = 1400$ nm. By comparing Figs. 7(c) and 7(d), we can observe that the first higher-energy peak originates from the direct electrons and the second higher-energy peak originates from both the direct electrons and the rescattering electrons. In order to better illustrate the physical origin of the second higher-energy peak shown in Fig. 7 and the stronger distribution in the relative high-energy region shown in Fig. 2(b4), we mainly focus on the rescattering electron in this paper.

Initial transverse momentum distribution of the electrons plays an important role in the course of tunneling ionization

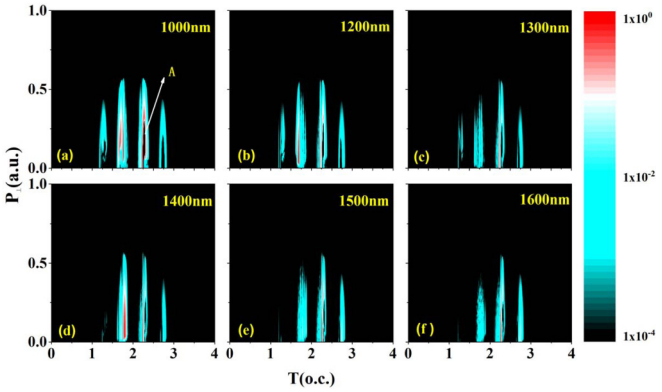

FIG. 8. Initial transverse momentum of photoelectrons as a function of the ionization time for different laser wavelengths in the spatially inhomogeneous field ($\varepsilon = 0.003$).

[38,44,48]. Figure 8 shows the initial transverse momentum of photoelectrons as a function of the ionization time for different laser wavelengths in the spatially inhomogeneous field ($\varepsilon = 0.003$). From Fig. 8(a), we can see that the initial transverse momentum distribution of each half cycle is similar. Significantly, the missing area as indicated by "A" in the second half cycle is due to the trapping of the electrons by the parent ions and those electronic wave packets can be stabilized in the Rydberg states [38,44].

With the increase of the laser wavelength, the initial transverse momentum in the second half cycle is stronger than that in the first half cycle as shown in Figs. 8(a)–8(c) and Figs. 8(e) and 8(f). This result explains why the PMD in the low-energy region is significantly stronger than that in the high-energy region with the increase of the laser wavelength as shown in Figs. 2(b1)–2(b3) and Figs. 2(b5) and 2(b6). However, Fig. 8(d) shows that the initial transverse momentum for the critical wavelength $\lambda = 1400$ nm is abnormal, which indicates that the PMD in the first half cycle is stronger than that in the second half cycle. From Fig. 5, we know that the rescattering electrons originate from the first half cycle and contribute to the relative high-energy region. In addition, from Fig. 7, we can find that the second higher-energy peak is closely related to the rescattering electrons, and the ionization rate of the rescattering electrons increases for the critical wavelength $\lambda = 1400$ nm. Therefore, for the critical wavelength $\lambda = 1400$ nm as shown in Fig. 8(d), the abnormal phenomenon is due to the high-energy rescattering electrons. It is proved once again that the stronger distributions in the relative high-energy region shown in Fig. 2(b4) are controlled by the rescattering electrons in the first half cycle and the distributions are sensitive to the initial transverse momentum of the rescattering electrons.

In addition, we investigate the influence of the inhomogeneity parameter on the wavelength dependence of PMDs for the laser wavelength $\lambda = 1400$ nm as shown in Fig. 9. We have chosen the different inhomogeneity parameters. We can clearly see that the inhomogeneous character of the laser field has a strong modification on PMDs and the critical wavelength mentioned earlier is associated to the inhomogeneity parameter. For the inhomogeneity parameter $\varepsilon = 0.002$ as shown in Fig. 9(a), the relative high-energy region and the relative low-energy region are not completely separated. For the inhomogeneity parameter $\varepsilon = 0.003$ as shown in Fig. 9(b), the relative high-energy region and the relative low-energy region are just separated. However, for the inhomogeneity parameter $\varepsilon = 0.004$ as shown in Fig. 9(c), the separation of the relative high-energy region and the relative low-energy region is obvious. It is indicated that the critical wavelength is gradually decreased as the inhomogeneity parameter ε increases.

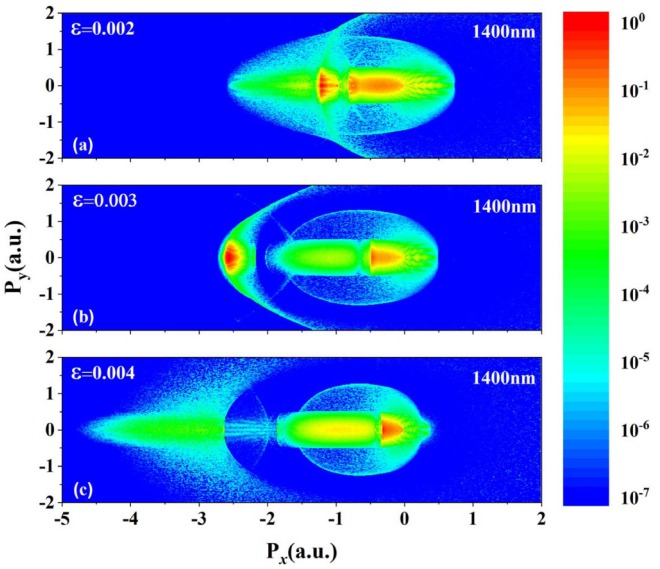

FIG. 9. Two-dimensional photoelectron momentum distributions for the laser wavelength and different inhomogeneity parameters. (a) $\varepsilon = 0.002$, (b) $\varepsilon = 0.003$, and (c) $\varepsilon = 0.004$.

IV. CONCLUSIONS

In summary, we theoretically investigate the wavelength dependence of the photoelectron momentum distribution in the inhomogeneous field by the ISCTS model. The photoelectron momentum distribution can be separated into two regions when the wavelength reaches a certain value in the inhomogeneous field, which is called the critical wavelength. The wavelength is longer than the critical wavelength, and the rescattering energy of the electron is greatly enhanced. Based on the electron orbits analysis, we demonstrate that the high-energy region mainly originates from the short orbit of the rescattering electrons. We also demonstrate that the holographic interference structure can be isolated in the inhomogeneous field. And the holographic interference structure of the shorter wavelength is more obvious than that of the longer wavelength. Our results may provide a reference for further analytical research of the holographic interference of both experiments and theories in the inhomogeneous field. In addition, the prominent high-energy peak is sensitive to the initial transverse momentum of the rescattering electrons after tunneling. We also demonstrate that the critical wavelength is gradually decreased as the inhomogeneity parameter ε increases.

ACKNOWLEDGMENT

This work was supported by the National Natural Science Foundation of China (Grant No. 12074142).

[1] P. Agostini, F. Fabre, G. Mainfray, G. Petite, and N. K. Rahman, Phys. Rev. Lett. **42**, 1127 (1979).

[2] L. V. Keldysh, Zh. Eksp.Teor. Fiz. **47**, 1945 (1964) [Sov. Phys. JETP **20**, 1307 (1965)].

[3] G. G. Paulus, W. Nicklich, H. Xu, P. Lambropoulos, and H. Walther, Phys. Rev. Lett. **72**, 2851 (1994).

[4] C. Wang, X. Li, X.-R. Xiao, Y. Yang, S. Luo, X. Yu, X. Xu, L.-Y. Peng, Q. Gong, and D. Ding, Phys. Rev. Lett. **122**, 013203 (2019).

[5] L. Guo, S. Chen, M. Liu, Z. Shu, S. Hu, R. Lu, S. Han, and J. Chen, Phys. Rev. A **101**, 033415 (2020).

[6] X.-X. Huo, Y.-H. Xing, T. Qi, Y. Sun, B. Li, J. Zhang, and X.-S. Liu, Phys. Rev. A **103**, 053116 (2021).

[7] M. Ferray, A. L'Huillier, X. F. Li, L. A. Lompre, G. Mainfray, and C. Manus, J. Phys. B: At. Mol. Opt. Phys. **21**, L31 (1988).

[8] M. A. Khokhlova, M. Y. Emelin, M. Y. Ryabikin, and V. V. Strelkov, Phys. Rev. A **103**, 043114 (2021).

[9] P. M. Paul, E. S. Toma, P. Breger, G. Mullot, F. Augé, Ph. Balcou, H. G. Muller, and P. Agostini, Science **292**, 1689 (2001).

[10] D. N. Fittinghoff, P. R. Bolton, B. Chang, and K. C. Kulander, Phys. Rev. Lett. **69**, 2642 (1992).

[11] S. Ben, T. Wang, T.-T. Xu, J. Guo, and X.-S. Liu, Opt. Express **24**, 7525 (2016).

[12] T.-T. Xu, S. Ben, T. Wang, J. Zhang, J. Guo, and X.-S. Liu, Phys. Rev. A **92**, 033405 (2015).

[13] N. Li, Y. Zhou, X. Ma, M. Li, C. Huang, and P. Lu, J. Chem. Phys. **147**, 174302 (2017).

[14] P. B. Corkum, Phys. Rev. Lett. **71**, 1994 (1993).

[15] P. Salieres, B. Carré, L. L. Déroff, F. Grasbon, G. Paulus, H. Walther, R. Kopold, W. Becker, D. B. Milošević, A. Sanpera, and M. Lewenstein, Science **292**, 902 (2001).

[16] X.-B. Bian, Y. Huismans, O. Smirnova, K.-J. Yuan, M. J. J. Vrakking, and A. D. Bandrauk, Phys. Rev. A **84**, 043420 (2011).

[17] D. G. Arbó, K. L. Ishikawa, E. Persson, and J. Burgdörfer, Nucl. Instrum. Methods Phys. Res. Sect. B **279**, 24 (2012).

[18] F. Lindner, M. G. Schätzel, H. Walther, A. Baltuška, E. Goulielmakis, F. Krausz, D. B. Milošević, D. Bauer, W. Becker, and G. G. Paulus, Phys. Rev. Lett. **95**, 040401 (2005).

[19] Y. Huismans, A. Rouzée, A. Gijsbertsen, J. H. Jungmann, A. S. Smolkowska, P. S. W. M. Logman, F. Lépine, C. Cauchy, S. Zamith, T. Marchenko *et al.*, Science **331**, 61 (2011).

[20] M. Li, W.-C. Jiang, H. Xie, S. Luo, Y. Zhou, and P. Lu, Phys. Rev. A **97**, 023415 (2018).

[21] S. D. López and D. G. Arbó, Phys. Rev. A **100**, 023419 (2019).

[22] S. Kim, J. Jin, Y.-J. Kim, I.-Y. Park, Y. Kim, and S.-W. Kim, Nature (London) **453**, 757 (2008).

[23] A. Husakou, S.-J. Im, and J. Herrmann, Phys. Rev. A **83**, 043839 (2011).

[24] M. F. Ciappina, J. A. Pérez-Hernández, T. Shaaran, J. Biegert, R. Quidant, and M. Lewenstein, Phys. Rev. A **86**, 023413 (2012).

[25] X.-Y. Luo, T. Wang, Q. Wang, and X.-S. Liu, Laser Phys. **26**, 115301 (2016).

[26] M. F. Ciappina, J. Biegert, R. Quidant, and M. Lewenstein, Phys. Rev. A **85**, 033828 (2012).

[27] J. Wang, G. Chen, S.-Y. Li, D.-J. Ding, J.-G. Chen, F.-M. Guo, and Y.-J. Yang, Phys. Rev. A **92**, 033848 (2015).

[28] J. Luo, Y. Li, Z. Wang, Q. Zhang, and P. Lu, J. Phys. B: At. Mol. Opt. Phys. **46**, 145602 (2013).

[29] P. Rueda, F. Videla, E. Neyra, J. A. Pérez-Hernández, M. F. Ciappina, and G. A. Torchia, J. Phys. B: At. Mol. Opt. Phys. **53**, 065403 (2020).

[30] L. Ortmann, J. A. Pérez-Hernández, M. F. Ciappina, J. Schötz, A. Chacón, G. Zeraouli, M. F. Kling, L. Roso, M. Lewenstein, and A. S. Landsman, Phys. Rev. Lett. **119**, 053204 (2017).

[31] M. F. Ciappina, J. A. Pérez-Hernández, T. Shaaran, L. Roso, and M. Lewenstein, Phys. Rev. A **87**, 063833 (2013).

[32] Y. Chen, Y. Zhou, J. Tan, M. Li, W. Cao, and P. Lu, Phys. Rev. A **104**, 043107 (2021).

[33] Y. Sun, S. Ben, J. H. Chen, Q. Zhen, and X. S. Liu, Europhys. Lett. **135**, 13001 (2021).

[34] Y. Huismans, A. Gijsbertsen, A. S. Smolkowska, J. H. Jungmann, A. Rouzée, P. S. W. M. Logman, F. Lépine, C. Cauchy, S. Zamith, T. Marchenko, J. M. Bakker, G. Berden, B. Redlich, A. F. G. van der Meer, M. Y. Ivanov, T.-M. Yan, D. Bauer, O. Smirnova, and M. J. J. Vrakking, Phys. Rev. Lett. **109**, 013002 (2012).

[35] L. He, Z. Wang, Y. Li, Q. Zhang, P. Lan, and P. Lu, Phys. Rev. A **88**, 053404 (2013).

[36] G. Herink, D. R. Solli, M. Gulde, and C. Ropers, Nature (London) **483**, 190 (2012).

[37] X.-Y. Wu, H. Liang, M. F. Ciappina, and L.-Y. Peng, Photonics **7**, 129 (2020).

[38] M. Li, J.-W. Geng, H. Liu, Y. Deng, C. Wu, L.-Y. Peng, Q. Gong, and Y. Liu, Phys. Rev. Lett. **112**, 113002 (2014).

[39] N. I. Shvetsov-Shilovski, M. Lein, L. B. Madsen, E. Räsänen, C. Lemell, J. Burgdörfer, D. G. Arbó, and K. Tőkési, Phys. Rev. A **94**, 013415 (2016).

[40] B. Krässig, M. Jung, D. S. Gemmell, E. P. Kanter, T. LeBrun, S. H. Southworth, and L. Young, Phys. Rev. Lett. **75**, 4736 (1995).

[41] C. T. L. Smeenk, L. Arissian, B. Zhou, A. Mysyrowicz, D. M. Villeneuve, A. Staudte, and P. B. Corkum, Phys. Rev. Lett. **106**, 193002 (2011).

[42] M. V. Ammosov, N. B. Delone, and V. P. Krainov, Zh. Eksp. Teor. Fiz. **91**, 2008 (1986) [Sov. Phys. JETP **64**, 1191 (1986)].

[43] N. B. Delone and V. P. Krainov, J. Opt. Soc. Am. B **8**, 1207 (1991).

[44] H. Liu, Y. Liu, L. Fu, G. Xin, D. Ye, J. Liu, X. T. He, Y. Yang, X. Liu, Y. Deng, C. Wu, and Q. Gong, Phys. Rev. Lett. **109**, 093001 (2012).

[45] M.-H. Yuan, A. D. Bandrauk, and X.-B. Bian, Phys. Rev. A **103**, 013108 (2021).

[46] I. Yavuz, E. A. Bleda, Z. Altun, and T. Topcu, Phys. Rev. A **85**, 013416 (2012).

[47] L. Ortmann and A. S. Landsman, Phys. Rev. A **97**, 023420 (2018).

[48] Y. Shao, Z. Yuan, D. Ye, L. Fu, M.-M. Liu, X. Sun, C. Wu, J. Liu, Q. Gong, and Y. Liu, J. Opt. **19**, 124004 (2017).